4

Hybrid Model Approaches to Predict Multiscale and Multiphysics Coastal Hydrodynamic and Sediment Transport Processes

H. S. Tang[1,*] and Timothy Keen[2]
[1]*City College, City University of New York*
[2]*Naval Research Laboratory*
USA

1. Introduction

Coastal ocean processes are complicated and they happen as various phenomena that span a vast range of spatial and temporal scales. For instance, general circulations of oceans occur at global scales (Wunsch & Ferrari, 2004). Tropical waves that eventually impact coastal waters propagate with wavelengths of one thousand kilometers and periods of one month (Legeckis et al., 1983). Langmuir cells, which are pairs of vortices hanging below water surfaces, have spatial sizes ranging from one to hundreds of meters (Weller et al., 1985). Scour near coastal structures is under influence of large-scale current processes but occurs in a relatively small size (Sumer & Whitehouse, 2001). Flows around enormous numbers of swimming microorganisms can occur at scales of micrometers (Pedley, 1992). Here, the scales are either observation scales such as characteristic length and time or process scales such as those in wavelet analysis (Chui, 1992; Kumar and Foufoula-Georgiou, 1997).

Since a few decades ago, various geophysical fluid dynamics (GFD) models have been developed for individual coastal ocean phenomena at specific scales. The Princeton Ocean Model (POM), Finite-Volume Coastal Ocean Model (FVCOM), and HYbrid Coordinate Ocean Model (HYCOM) were developed to predict current velocity, sea level, salinity, and temperature at regional scales (Blumberg and Mellor, 1987; Chen et al., 2003; Halliwell, 2004). The WAVEWATCH and SWAN (Simulating Waves Nearshore) models were designed to simulate surface wave propagation at global to coastal scales (Tolman, 1991; Booij et al., 1999). Models have also been proposed to predict sediment transport and seabed morphology for near-coastal regions (e.g., Tonnon et al., 2007; Papanicolaou et al., 2008). In recent years, computational fluid dynamics (CFD), which can accurately model small-scale and detailed flow structures, has been applied to coastal engineering flows (e.g., Young et al., 2001). In view of the multiscale and multiphysics nature of coastal ocean processes, there is a great challenge to simulate them accurately and, until now, the efforts using numerical simulation have been successful merely for individual phenomena and scales. The challenge comes from model restrictions, numerical techniques, and computer capabilities. For

* Changsha University of science and Technology, China

instance, a deep-ocean model has difficulty in dealing with the vertical mesh at sudden bathymetry changes as well as the smaller scales of nearshore flows (Song & Hou, 2006; Heimusund & Berntsen, 2004). Limitations such as hydrostatic assumptions and/or two-dimensionality of GFD models are inherent restrictions that prohibit accurate simulations of many important phenomena such as vertical motions of Langmuir cells. It is frequently reported that coastal models become unstable at small time steps and grid spacing (e.g., Heimusund & Berntsen, 2004; Keen et al., 2003), which is not a surprise since they are designed for large-scale flow phenomena. It is anticipated that the solutions of the models do not necessarily converge to those of Navier-Stokes equations as grid spacing tends to zero. Therefore, it is not realistic to achieve accurate simulation of coastal phenomena, especially the small-scale processes, by just using existing coastal ocean models and simply reducing time steps and grid spacing. Although in principle CFD approaches have fewer limitations and can capture flow phenomena at much broader spectra of scales, they are computationally expensive and not applicable in simulating a complete actual coastal ocean flow. It should be noted that, although both GFD and CFD are based on the Navier-Stokes equations, they are different approaches with respect to numerical technique, turbulence closure, and parameterization for small scales.

It is now becoming a trend in prediction of coastal ocean flows to adapt to multiphysics/multiscale approaches (Fringer et al., 2006). Although computer modeling has reached the point where the simulation of individual flow phenomena over relatively narrow ranges of scales has become mature, a single, comprehensive model capable of dealing with multiphysics/multiscale problems is unlikely to be available in the near future. The hybrid method (HM) couples different models to each other, and the domain decomposition method (DDM) divides a flow domain into many subdomains, each of which is assigned to an individual model. Combining HM and DDM is one of the most promising currently available techniques to bridge the scales and overcome difficulties in multiphysics/multiscale modeling (Benek et al., 1983; Harten, 1993; Dolbow et al., 2004).

Since erosion and transport of erodible seabed sediment is coupled to various hydrodynamic forces, it is imperative to analyze them at different scales in correspondence to multiscale hydrodynamic processes (Chiew, 1991). It has been common to assume that seabed scour is a local process, which occurs within a few tens of diameters of a structure resting on the seafloor (Zang et al., 2009). This is true for event-scale erosion but it is unlikely for systematic or catastrophic scour and/or burial processes that operate at months or yearly time scales. Experimental results and parametric methods for scour around structures on the seafloor have been supplemented by numerical models that focus on the finest scales around the obstacles (Alam & Cheng, 2010). These high-resolution models typically focus on steady flow but recent laboratory studies have examined wave-induced scour (Xu et al., 2009) and numerical methods have been applied to shoaling waves (Myrhaug et al., 2008). These studies use simplified hydrodynamic forcing because of the disparity in scales between the external (ocean currents) and internal flows (around structures).

CFD approaches for the fluid flow around a structure are not easily implemented for sediments because of the interaction of turbulence with discrete particles. Thus, scour models have traditionally used parametric approaches (Myrhaug et al., 2008) and discrete particle models (Zamankhan & Doolatshahi, 2008). Lattice Boltzmann methods are being explored as well for simple geometries (Alam & Cheng, 2010). These approaches depend on a given flow field that is typically simplified from the ocean environment. The constitutive equations for these models are derived from observations in flumes and the seabed, and

thus are specifically formulated for near-field flow. The other extreme is to use a numerical model of regional flow to calculate a large-scale mean scour that can be used as an indicator of variations in potential scour within a selected region (Keen & Glenn, 2002). These models tend to use the same macroscopic approach represented by the Navier-Stokes equations. There is a lack of knowledge of the impact of these external hydrodynamic processes on the local scour and burial problem. In order to use localized scour models to investigate the impact of external factors on seabed scour, it is necessary to implement them on much larger domains. This approach is problematic with current computational resources. The problem of applying a macroscopic model (i.e., those based on Navier-Stokes equations) for the external problem and a scour model for the local scour is prohibitive because of fundamental differences in their numerical formulations. This problem can be more easily examined using macroscopic approaches, which have common numerical formulations and parameterizations.

This chapter summarizes our recent work in modeling of multiscale and multiphysics hydrodynamics phenomena using HM and DDM. We also discuss related sediment transport, with emphasis on localized scour and erosion processes. First, a hybrid approach that couples the FVCOM and a CFD model is described, and results of multiscale simulation for an effluent thermal discharge from a diffuser at the ocean bottom is presented. Second, an analysis is made of the effects of local-scale hydrodynamics on sediment transport around the diffuser. Third, as a multiphysics modeling of interaction between different phenomena, simulation of flow over sand dunes under action of surface wind is presented to illustrate the interaction between surface waves, currents, and morphology. These examples demonstrate the multiscale/multiphysics methodology as applied to problems that cannot be simulated as either local or external phenomena. They also indicate that multiscale and multiphysics simulations of hydrodynamics are more advanced than conventional modeling because of the complex interaction between the flow and discrete particles in the ocean.

2. Hybrid CFD and FVCOM for simulation of thermal effluent into coastal flows

A well-tested CFD model is employed in this work (Lin & Sotiropoulos, 1997; Tang et al., 2003; Tang et al., 2008). The governing equations for hydrodynamic processes of the CFD model are the three-dimensional (3D) continuity and Navier-Stokes equations that, in general curvilinear coordinates, are expressed as follows:

$$\Gamma \frac{\partial Q}{\partial t} + J \frac{\partial}{\partial \xi^k}(F^k - F_v^k) + I = 0, \tag{1}$$

where

$$\Gamma = diag(0,1,1,1), \qquad Q = (p,u,v,w)^T,$$

$$F^k = \frac{1}{J}(U^k, uU^k + p\xi_x^k, vU^k + p\xi_y^k, wU^k + p\xi_z^k)^T, \tag{2}$$

$$F_v^k = \frac{1}{J}\left(\frac{1}{\mathrm{Re}} + \nu_t\right)(0, g^{lk}\frac{\partial u}{\partial \xi^l}, g^{lk}\frac{\partial v}{\partial \xi^l}, g^{lk}\frac{\partial w}{\partial \xi^l})^T,$$

$$I = -\frac{T}{Fr^2}e,$$

where: t is time; $J = |\partial x_i / \partial \xi^j|$ is the Jacobian of the geometric transformation from Cartesian coordinates, x_i (i = 1, 2, 3 for x, y, z axes, respectively) to curvilinear coordinates ξ^j (j = 1, 2, 3); p is the static pressure divided by the density; u, v, and w are the velocities in x, y, and z directions, respectively; T is the temperature. Furthermore, $U^k = u_i \xi^i_{x_k}$ are the contravariant velocities in ξ^k directions (Note that u_i are, respectively, u, v, and w, $\xi^i_{x_k}$ are the metrics of the geometric transformation, and repeated indices imply summation); Re is the Reynolds number; ν_t is turbulence eddy viscosity; g^{ij} ($g^{ij} = \xi^i_{x_k} \xi^j_{x_k}$) is the contravariant metric tensor; Fr is Froude number; e is the unit in the gravity direction. The governing equation for heat transfer reads as

$$\frac{1}{J}\frac{\partial T}{\partial t} - \frac{\partial}{\partial \xi^k}\left\{\frac{1}{J}\left(\frac{1}{\mathrm{Pr}\,\mathrm{Re}} + \frac{\nu_t}{\mathrm{Pr}_t}\right) g^{lk}\frac{\partial T}{\partial \xi^l}\right\} = 0 . \tag{3}$$

where: Pr is the molecular Prandtl number; Pr_t is the turbulent Prandtl number; l = 1, 2, 3. The standard mixing length model is used in this work (Mason, 1989). The governing equations are discretized using a second-order accurate, implicit, finite-volume method on non-staggered grids, and they are solved using a dual time-stepping artificial compressibility method. A fourth-difference artificial dissipation method and V-cycle multigrid method are used. A domain decomposition method in conjunction with the Schwartz alternative iteration is employed to deal with complicated geometry. In order to achieve seamless transition of solutions between subdomains, an effective mass conservation algorithm is proposed. The CFD model has been tested and applied in various problems from academe as well as industry, such as vortex breakdown and flow past bridge piers (Sotiropoulos and Ventikos, 1998; Ge and Sotiropoulos, 2005). For details of the CFD model, readers are referred to Lin & Sotiropoulos (1997), Tang et al. (2003; 2008), and Xu & Sun (2009).

In the FVCOM, the governing equations are the continuity and momentum equations. The governing equations for the external mode in the model are vertically averaged two-dimensional (2D) continuity and momentum equations. The 2D continuity equation is (Chen et al., 2006):

$$\frac{\partial \eta}{\partial t} + \frac{\partial H U_l}{\partial x_l} = 0 , \tag{4}$$

where: η is the water surface elevation; H is water depth; and U_l are depth-average current velocities in x_l directions. The momentum equations are:

$$\begin{aligned}\frac{\partial U_i H}{\partial t} + \frac{\partial U_i U_l H}{\partial x_l} = -gH\frac{\partial \eta}{\partial x_i} - \frac{gH}{\rho_0}\left(\int_{-1}^{0}\frac{\partial}{\partial x_i}\left(H\int_{\sigma}^{0}\rho d\sigma'\right)d\sigma + \frac{\partial H}{\partial x_i}\int_{-1}^{0}\sigma\rho d\sigma\right) \\ + (-1)^i f U_j H + \frac{\tau_{sx_i} - \tau_{bx_i}}{\rho_0} + D\tilde{F}_i + G_i ,\end{aligned} \tag{5}$$

$$G_i = \frac{\partial U_i U_l H}{\partial x_l} - D\tilde{F}_i - \left(\frac{\partial \overline{u_i u_l} H}{\partial x_l} - D\overline{F}_i\right),$$

$$D\tilde{F}_i \approx \frac{\partial}{\partial x_l}\left(\bar{A}_m D\left(\frac{\partial U_i}{\partial x_l}+\frac{\partial U_l}{\partial x_i}\right)\right),\ D\bar{F}_i \approx \frac{\partial}{\partial x_l}\overline{\left(A_m D\left(\frac{\partial u_i}{\partial x_l}+\frac{\partial u_l}{\partial x_i}\right)\right)}, \tag{6}$$

where: the overbar denotes the vertical integration; g is the gravity constant; ρ_0 is the reference density of seawater; σ is vertical coordinate; f is the Coriolis parameter; τ_{sx_i} are the surface friction stresses, and τ_{bx_i} are the bottom friction stresses in x_i directions; D is the mean water depth; and A_m is the horizontal eddy viscosity (Smagorinsky, 1963). The governing equations of the internal mode in the model are 3D continuity and momentum equations with x and y as horizontal coordinates and σ as vertical coordinate:

$$\frac{\partial \eta}{\partial t}+\frac{\partial H u_l}{\partial x_l}+\frac{\partial \omega}{\partial \sigma}=0, \tag{7}$$

$$\begin{aligned}\frac{\partial u_i H}{\partial t}+\frac{\partial u_i u_l H}{\partial x_l}+\frac{\partial u_i \omega}{\partial \sigma} = &-gH\frac{\partial \eta}{\partial x_i}-\frac{gH}{\rho_0}\left(\frac{\partial}{\partial x_i}\left(H\int_\sigma^0 \rho d\sigma'\right)+\sigma\rho\frac{\partial H}{\partial x_i}\right)\\ &+(-1)^i f u_j H+\frac{1}{H}\frac{\partial}{\partial \sigma}\left(K_m\frac{\partial u_i}{\partial \sigma}\right)+DF_i,\end{aligned} \tag{8}$$

$$DF_i \approx \frac{\partial}{\partial x_l}\left(A_m D\left(\frac{\partial u_i}{\partial x_l}+\frac{\partial u_l}{\partial x_i}\right)\right), \tag{9}$$

where: u_i are the layer horizontal velocity components; ω is the vertical velocity in σ coordinate; and K_m is the vertical eddy viscosity, which is determined using the Mellor and Yamada level-2.5 turbulent closure (Mellor & Yamada, 1982; Chen et al., 2003). In the FVCOM: i, j, l=1, 2 ($i \neq j$). The governing equations are discretized using a finite-volume method with triangle meshes on horizontal planes and layer meshes in the vertical direction. Second-order accurate upwind schemes are used to discretize the advection terms, and Runge-Kutta methods are employed to march in time. The external and internal modes may have different time steps. Mainly because it uses unstructured meshes, the FVCOM is becoming popular in coastal ocean modeling. Details for the FVCOM can be found in Chen et al. (2003; 2006).

In order to simulate multiscale and multiphysics coastal hydrodynamic processes, we proposed HM and DDM approaches (Tang & Wu, 2010; Wu & Tang 2010). In particular, the CFD model is coupled with the FVCOM; the CFD model is employed to resolve small-scale flow phenomena, and the FVCOM is used to model background circulation. The domains of the CFD model and FVCOM overlap over a region (Fig. 1). As a coupling strategy, the 3D CFD model is coupled to the 3D internal mode of the FVCOM, and the two models exchange solutions for the velocity distributions at grid interfaces between them. The strategy is based on the assumption that the obstacle covered by the CFD model only alters local velocity distribution but does not affect horizontal average velocities and water surface elevation, which are determined by the external mode. This assumption is consistent with the assumption in the FVCOM (Chen et al., 2003). Since Chimera grids (grids overlapping arbitrarily with each other) provide the best possible flexibility in connecting different models, we employed them to connect the CFD model and the FVCOM, as shown in Fig. 2. In the figure, a-b-c and d-e-f are grid interfaces between CFD model and FVCOM, and linear interpolations are made to provide solutions for velocities at the nodes and elements on the interfaces. The details of the coupling methods can be found in Tang & Wu (2010) and Wu & Tang (2010).

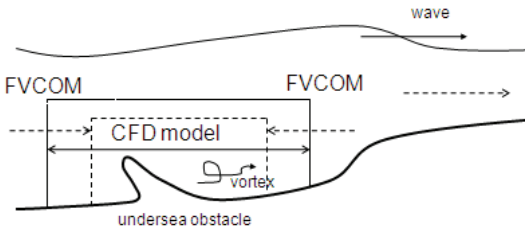

Fig. 1. Schematic representation of CFD model and FVCOM coupling.

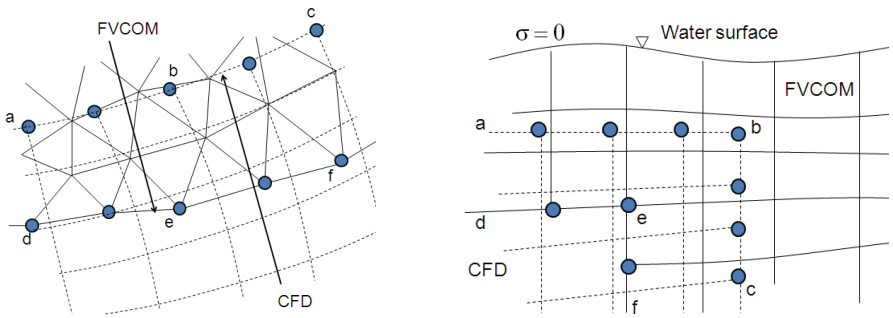

(a) (b)

Fig. 2. Layout of grids of CFD and FVCOM. Solid lines – FVCOM grid, dash lines – CFD grid. a) Horizontal plane grids. b) Vertical direction grids.

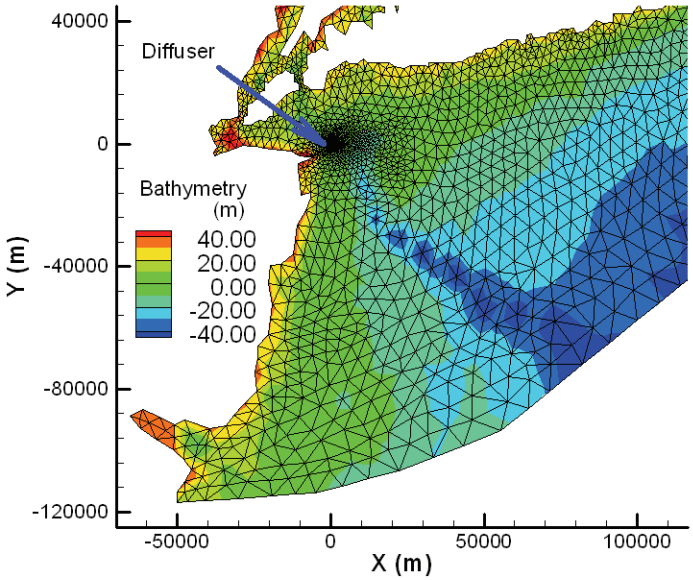

Fig. 3. Region of study, bathymetry, FVCOM mesh, and diffuser location.

Consider an effluent discharge from a diffuser in the setting of the New York and New Jersey coastal region under action of tides (Fig. 3). The x axis is in the east direction, and y axis is in the north direction. The diffuser is located in the New York Bight. The diffuser consists of a pipe with a diameter of 1.32 m lying on the ocean bottom, and ten ports with diameters of 0.175 m (Fig. 4a). All of the ten ports have an angle of 110° with respect to the x axis and upward angles with respect to the x-y plane ranging evenly from 45° to 18° from the first port, located near the origin of the plane, to the last port. Hot water at 32.0 °C is discharged at speed 3.92 ms^{-1} from the ports into the coastal water at 20.5 °C. The only driving force of the flow is tides; wind and other factors are ignored. This is a multiscale flow; the thermal effluent happens at scales of the discharge ports and the pipe, while the unsteady tides occur at scales of the tides.

The hybrid approach is used to simulate the flow; the CFD model captures the flow around the effluent from the diffuser, and the FVCOM describes the background large-scale flows. The mesh of the FVCOM is shown in Fig. 3, and those of the CFD model for the diffuser are shown in Fig. 4b. The CFD model and modeling of such thermal discharges have been intensively tested and calibrated using other models and measurement data (Tang et al., 2008). The coupling approach has been also validated (Tang & Wu, 2010; Wu & Tang, 2010).

The computed solutions are shown in Figs. 5, 6, 7, and 8. Fig. 5 presents the large-scale coastal flows at ebb and flood tides obtained with the FVCOM. It is seen from the figure that there are many total velocity patches, in red and blue, at scales ranging from 10^4 to 10^5 m. The thermal discharge, located near $x, y = 0$, is at the edges of a relative high velocity patch. No solution details for flows around the diffuser are available from simulations of the FVCOM; however, the CFD model provides the details. For example, Fig. 6 presents velocity distribution at a plane 6 m above the diffuser. Due to the presence of the diffuser and thermal effluent, the flow field during both ebb and flood tides is greatly altered; there are several velocity patches at scales of 10 m and larger, together with a low-velocity region at downstream side of the diffuser, which runs from $x, y = 0$ to the northwest direction (Fig. 6). Especially, there is a large vortex right behind the diffuser in case of flood tides.

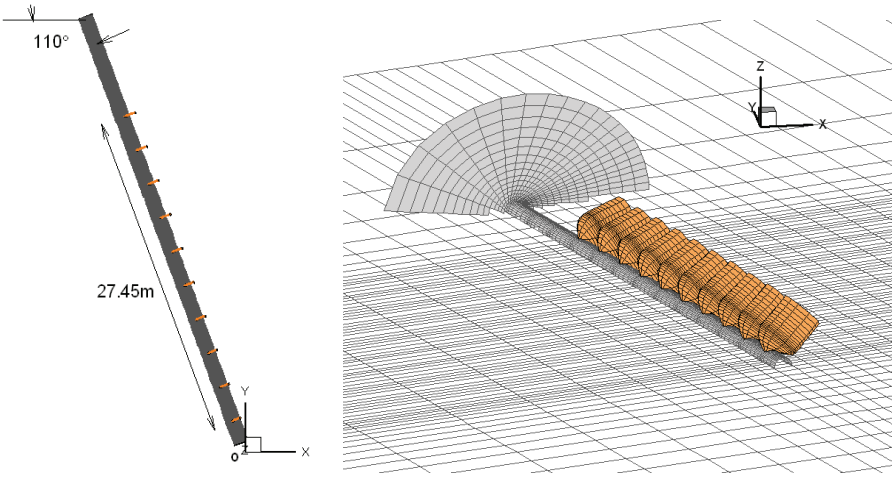

(a) (b)

Fig. 4. (a) Configurations of the diffuser. (b) CFD Meshes for the diffuser

As seen in Fig. 4a, the discharge ports point to the northeastern direction, and thus the hot water jets should be in the same direction. Fig. 7 indicates that during ebb tides, the jets are initially towards northeast but shortly later, due to the northwestern ambient tide currents, they turn towards the northwestern direction. While during flood tides, the jets and the currents are in about same directions, the thermal plume runs to a far downstream location. The CFD model has a high resolution at the mouth of the ports, with 10 grid nodes across the port diameter of order 1 cm resolution. As demonstrated in our previous studies (Tang et al., 2008), the CFD model accurately resolves velocities and temperature at the mouths of all ports using this mesh resolution.

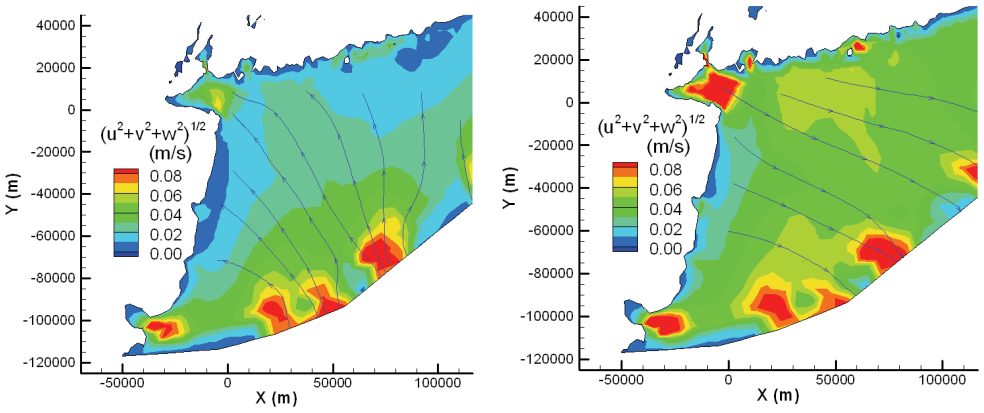

(a) (b)

Fig. 5. Large-scale surface velocity field at (a) flood tides and (b) ebb tides.

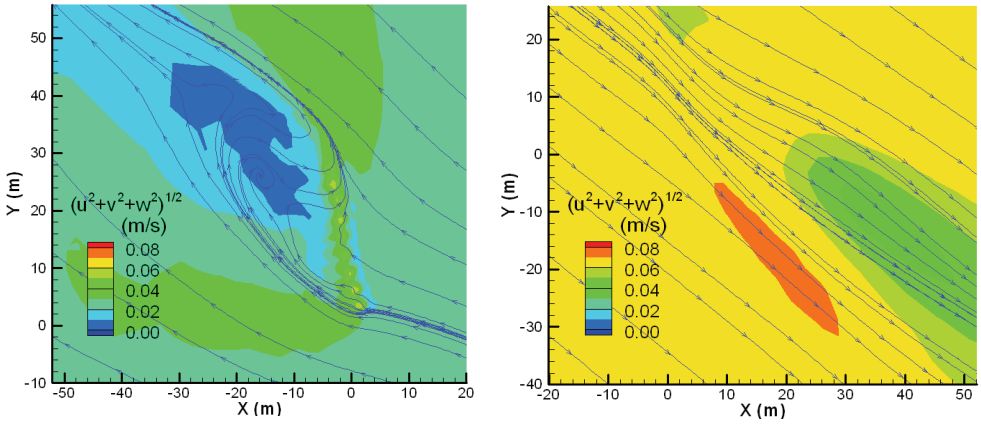

(a) (b)

Fig. 6. Local velocity on a plane 6 m above the diffuser at (a) flood and (b) ebb tide.

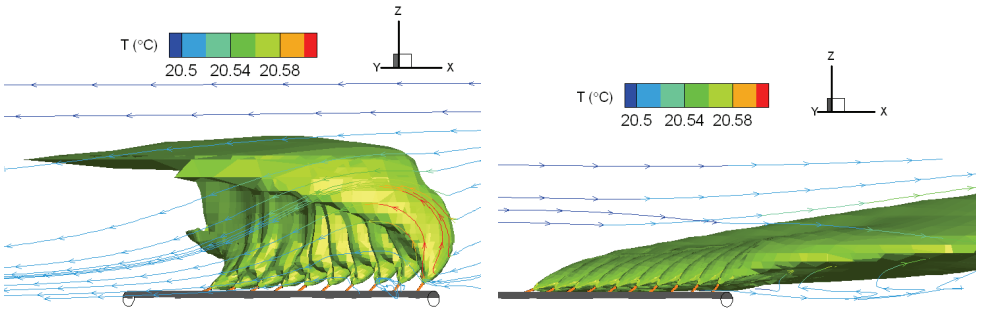

(a) (b)

Fig. 7. 3D temperature plume at (a) flood and (b) ebb tide.

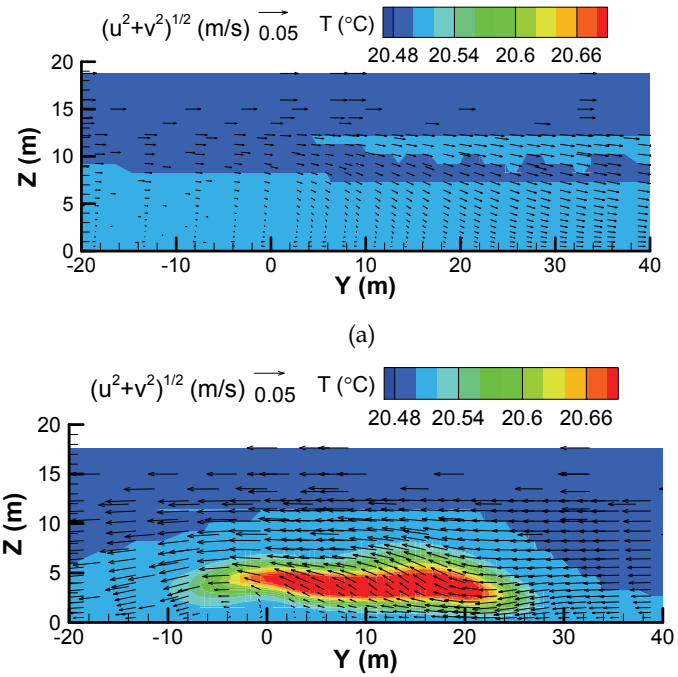

(a)

(b)

Fig. 8. Cross-section velocity and temperature at 10 m downstream from the diffuser in the x direction. (a) Flood tide. (b) Ebb tide.

Figure 8 shows the temperature and velocity field at a vertical cross-section, which is at the east side of diffuser. In case of the flood tides, the currents and thermal jets from all ports are in opposite directions and the thermal plume cannot reach this section whereas, for ebb tides, they are in the same directions and the plume is still strong on the section. In the latter case, the jets from individual ports already have merged with each other and no individual

plumes are observed, and this is the result of intensive mixing in the cross-section (Fig. 8b). As shown in Fig. 8, there are fast lateral currents along the cross-section. Due to interaction of the effluent flows and the cross-section currents, there are vertical vortices next to the head of the diffuser, located near $x, y = 0$. It should be noted that all these small structures of the flow and temperature fields are only captured by the CFD model, and they are not available from the FVCOM.

3. Scour around a diffuser at the seabed

This section discusses erosion and scour around the diffuser based on the modeling results for the multiscale hydrodynamic processes in the previous section. Including potential scour computations on all of these FVCOM and CFD grids is beyond the scope of the current work. Instead, the results of the flow field at 1 mab (meter above bed) from the overlapping grids are averaged for 1 m² boxes. The area of interest is centered on the diffuser and represented by a grid of 40 x 70 cells that are 1 m along each axis. The output from the different grids is available at a range of heights above the seafloor; we have chosen 1 m as the representative height for the shear stress computations. All of the grids are included in the average, which produces fields for the flood and the ebb tides.

No wave data are used in these hydrodynamic simulations, which aim only to show the influence of tidal flow. The sedimentation computations do not include advection and no sediment is transported; the plots thus show the equilibrium resuspension depth H_R as defined by Keen and Glenn (1998). These depths are a good indication of scour at shorter time scales. The scour depths shown in the plots represent the total that would occur over an approximately 1-hour period for which the bottom currents would be representative.

The mean currents during flood tide are very low but the distribution has additional structure not seen in the FVCOM output (Fig. 9a). A very similar pattern is predicted during ebb tide (Fig. 9b). This area is likely to be the focus for erosion. The bottom sediment at this general location is expected to be variable because of its proximity to the Hudson River Canyon and the resulting large sediment outflow from the Hudson River. The available sediment samples indicate available sediment from clay to sand (USGS 2010). We are using a representative sediment distribution of 20 classes ranging from 4 microns to 2000 microns (clay to gravel). The uniform sediment is represented by a mean of 100 microns (very fine sand) with a standard deviation of 40 microns. This specific sediment population includes 55% clay and 44% very fine sand, with < 1 % fine sand. The computed critical shear stresses are 0.465 and 0.4388 Pa, respectively for the dominant sizes.

Detailed simulations of erosion would require unavailable field data for the area. We are using the erosion rate formulation from Ariathurai et al (1983):

$$E_i = M\,(\tau_b \,/\, \tau_{c,i} - 1) \tag{10}$$

where: M is the entrainment rate; τ_b is the bottom shear stress; $\tau_{c,i}$ is the critical shear stress for entrainment of size class i. This formula is useful for adjusting entrainment for unknown areas. The value of M used in these simulations is 0.001 kg m^{-2} s^{-1}. The bottom shear stress is estimated from the common formulation:

$$\tau_b = \rho_w C_d (u^2+v^2) \tag{11}$$

where: ρ_w is the water density, which is set to1025 kg m^{-3}, and C_d is the coefficient of drag, which is set to 1. The large drag coefficient is necessary because the currents from the model were too low to exceed τ_c for the sediment used. Including wave effects would improve this

calculation. The resulting field of τ_b shows the effect of the diffuser (Fig. 10). Note that the bed stress is not symmetrical. Larger shear stresses are generated during the ebb tide and the pattern is slightly different from the flood. The persistent high shear stress is caused by the increased flow around the diffuser. This is partly attributable to the consistent seaward flow near x = -8 m during both flood and ebb tides, which is caused by a diffuser outflow of ~3.92 ms^{-1}. The diffuser flow is offshore, which appears to reinforce the ebb tide and make it more localized. This results in the concentration of higher stress around the outlets.

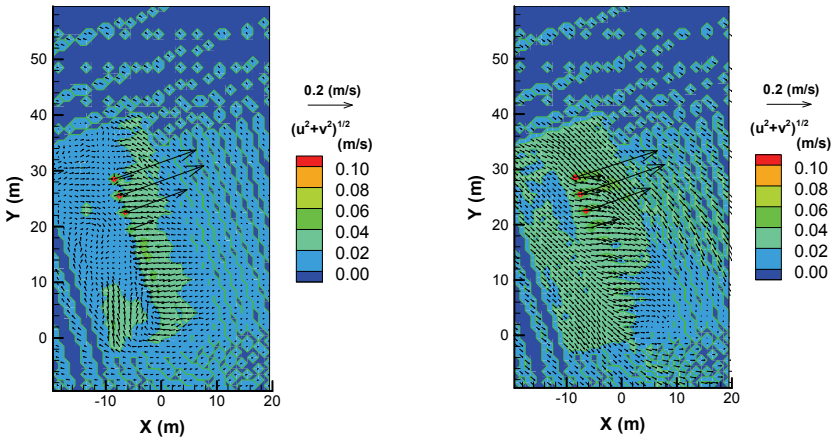

Fig. 9. Averaged currents from all CFD grids at 1 mab. (a) Flood tide; maximum velocity is 0.40223 m s^{-1}. (b) Ebb tide; maximum velocity is 0.40676 m s^{-1}.

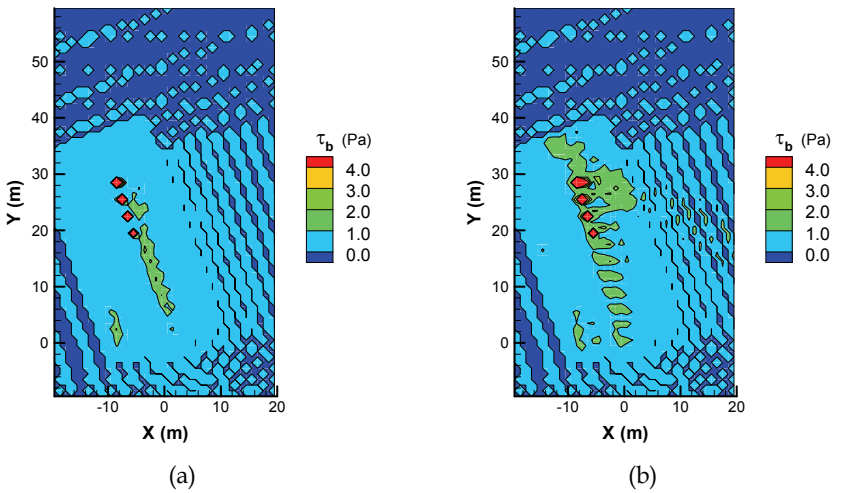

Fig. 10. Bottom drag calculated from Eq. (11). (a) Flooding tide; maximum shear stress is 165.83 Pa. (b) Ebb tide; maximum shear stress is 169.59 Pa.

The pattern of potential scour for the flood (Fig. 11a) and ebb (Fig. 11b) tides is reflective of the shear stresses. Note the greater scour seaward of the northern end of the diffuser during the ebb tide. This pattern is due to the fact that, as shown in Fig. 4a, the ports near the end have lower angles in comparison with the ports at the other end, and this leads to a stronger horizontal velocity and more intensive shearing at the end. These calculations of potential scour demonstrate the importance of calculating the detailed flow around the obstruction. No calculations were performed for the FVCOM flow fields because it provided uniform near-bottom flow with a small magnitude. These simulations suggest that there could be substantial scour and possible damage to the structure if not considered in its design. The scour depths would be greatly increased by the impact of storm waves 1-4 m high, which occur frequently during the fall and winter in the Middle Atlantic Bight (Keen & Glenn, 1995).

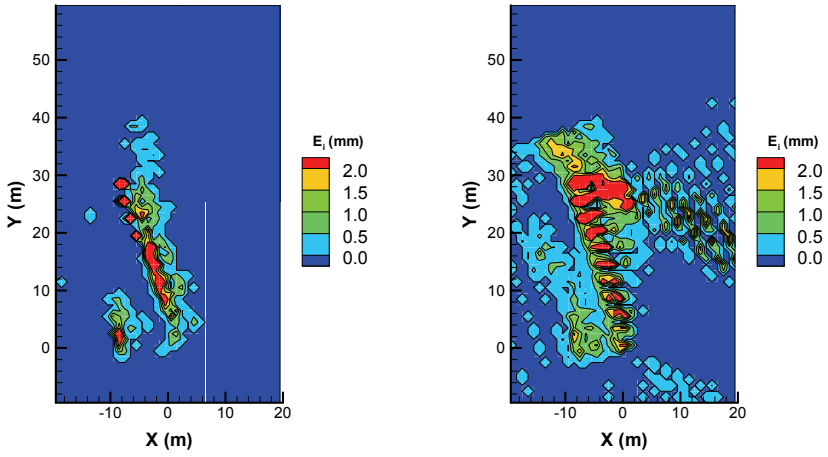

Fig. 11. Potential scour calculated from Eq. (10). (a) Flood tide; maximum erosion is 370.35 mm. (b) Ebb tide; maximum erosion is 378.76 mm.

4. Evolution of sand dunes under action of surface waves

The governing equation for wave action is given in a conservation form as (e.g., Mei, 1983):

$$\frac{\partial N}{\partial t}+\frac{\partial C_{gx_l}N}{\partial x_l}+\frac{\partial C_\sigma N}{\partial \sigma}+\frac{\partial C_\theta N}{\partial \theta}=\frac{S}{\sigma}, \tag{12}$$

where: t is the time; l =1, 2, and x_l correspond to x and y directions; σ is the frequency; and θ is the angle of the wave propagation direction; N is the wave action; C_{gx_l} are the wave speed in x_l direction in the physical space (x, y); C_σ and C_θ are, respectively, wave speed in σ and θ direction in the spectrum space (σ, θ); S is a source term that represents the combined effects of wind and other processes. In the current study, short waves are considered, which leads to a simple expression for C_{gx_l} (Mei, 1983).

The shallow water equations consist of the equation of mass conservation (e.g., Mei, 1983)

$$\frac{\partial H}{\partial t}+\frac{\partial HU_l}{\partial x_l}=0\,, \tag{13}$$

and the equations of momentum conservation:

$$\frac{\partial HU_i}{\partial t}+\frac{\partial HU_iU_l}{\partial x_l}=-gH\frac{\partial \eta}{\partial x_i}+\frac{\partial}{\partial x_i}\left(\nu_t H\left(\frac{\partial U_l}{\partial x_i}+\frac{\partial U_i}{\partial x_l}\right)\right)+\frac{\tau_{sx_i}-\tau_{bx_i}}{\rho}-\frac{1}{\rho}\frac{\partial S_{x_ix_l}}{\partial x_l}\,, \tag{14}$$

where: i,l =1, 2; ν_t is the turbulence eddy viscosity; ρ is the density; η is the water surface elevation; $S_{x_ix_l}$ are the radiation stresses resulting from waves.

The seabed morphology is controlled by the Exner equation (e.g., Henderson, 1966; Sleath, 1984):

$$\frac{\partial H_b}{\partial t}+\frac{\partial BU_l(U_1{}^2+U_2{}^2)^q}{\partial x_l}=0\,. \tag{15}$$

Here H_b is the elevation of the seabed, and B and q are constants. Typically, B depends on flow velocity, water depth, sediment grain sizes, and other factors, and q is usually in the range of $0.5\le q\le 1.5$. In this paper, q = 1 is used (Hudson & Sweby, 2005; Kubatko et al., 2006).

The interactions among waves, currents, and morphology can be seen in the governing equations. In Eq. (12), the wave action is related to wave speed C_{gx_l}; these are coupled with the current through the velocity U_l in Eq. (12) (Mei, 1983). As indicated in Eq. (14), the current is affected by the wave field through the radiation $S_{x_ix_l}$, and morphology evolution through bottom elevation H_b ($\eta=H+H_b$). Actually, the current is also affected by wind through the bottom stresses τ_{bx_i}. Morphology is directly related to the current through the velocity field as shown in Eq. (15). Details for the governing equations can be found in Tang et al. (2009).

Equations (12) through (15) comprise a coupled non-homogeneous system of conservation laws. Each component in the system reproduces the framework of well-known models. For instance, the wave action equation (12) is employed in SWAN (Booij et al., 1999), the shallow water equations (13) and (14) are used for SHORECIRC (Luettich and Westerink, 2004), and the morphology evolution equation (15) is also widely employed in engineering (e.g., Wu, 2004; Kubatko et al., 2006). In order to solve the system, an extension of the Lax-Friedrich scheme (Lax, 1954) is applied to discretize the wave action equation (12). Second, the MacCormack scheme (MacCormack, 1969) is employed to solve the shallow water equations. Finally, the fourth Euler scheme and central difference operator are used to solve the morphology equation. The coupled system and the code have been validated and calibrated using a series of problems. For details of the discretization, validation, and calibration, the readers are referred to Tang & et al. (2009).

The above coupled wave, current, and morphology system is applied to study evolution of sand dunes under action of surface waves on the horizontal plane. The initial conditions for the wave energy, the velocity field, and the bottom shape are, respectively

$$N=0, \tag{16a}$$

$$U_1=0,\ U_2=0,\ H=2-\sum_{i=1}^{n}\exp\left\{-0.01((x-0.5i)^2+y^2)\right\}, \tag{16b}$$

$$H_b=\sum_{m=1}^{n}\exp\left\{-0.01((x-0.5m)^2+y^2)\right\}, \tag{16c}$$

where n is the number of sand dunes. In this study, n = 1, 2, 3. The upstream boundary condition is

$$H=2\text{m},\quad x=-15\text{m}. \tag{17}$$

The wind effect is introduced as a source term in Eq. (12) at the upstream end:

$$S=0.15(1-\tanh(20+x-0.01t)), \tag{18}$$

which generates surface waves starting at the upstream end and propagating in the x direction. In the simulation, Δx, $\Delta y=0.4$ m, $\Delta\sigma=0.1$ s^{-1}, and $\Delta\theta$ =0.76 radians. Extrapolation is used to update solutions at the boundaries. Other related parameters are the same as those presented in our previous study on a single sand dune case (Tang et al., 2009).

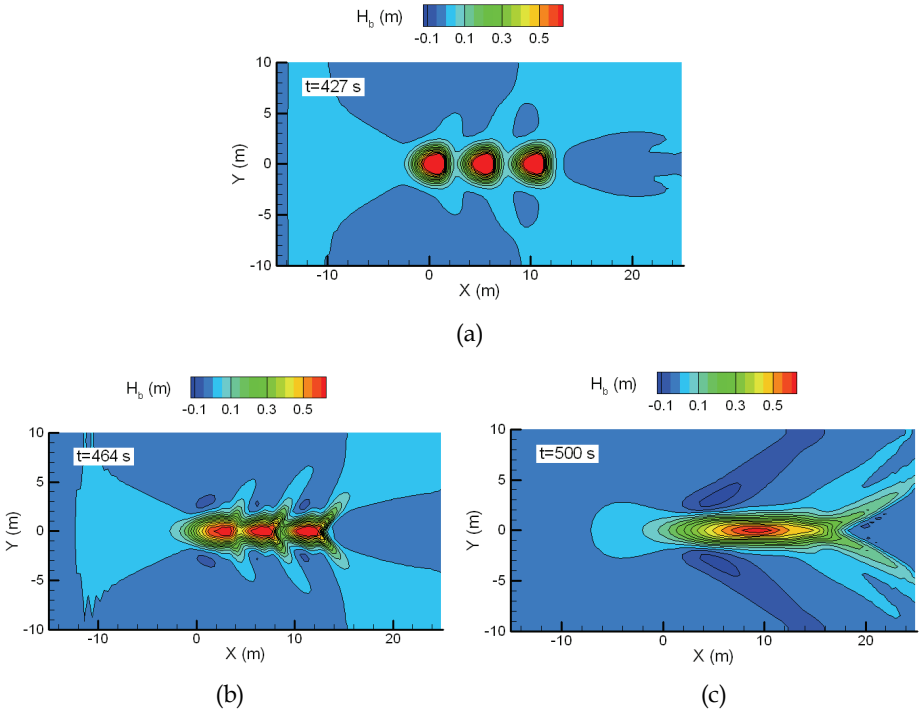

Fig. 12. Evolution of sand dunes (seabed elevation)

As seen in Eq. (18), the driving force S is a wave propagating in the x direction. The driving force generates a train of surface waves traveling in the same direction. The computed instantaneous evolution of sand dune elevation, surface height, and wave action, are

presented in Figs. 12 through 14 for three sand dunes (n=3). As shown in Fig. 12, as the wind blows from left to the right, all three sand dunes move in the x direction, and gradually they merge with each other. During this process, each sand dune is changing from a circle into a triangle, a steroidal, and then a strip, which are the three typical shapes of sand dunes in their evolution. At the same time, low-elevation regions are forming at the front, lateral sides, and immediately behind the three sand dunes. In Fig. 13, it is seen that the water surface has a bump in front and a dip behind each of the three dunes. In comparison with sand dune configurations in Fig. 12, it is known from Fig. 14 that wave action reaches minimums above all sand dunes and maximums right behind them. From Figs. 12 and 13 it is seen that, during the evolution of the sand dunes, both the wave field and water surface elevation evolve congruently with the sand dunes. Figure 14 reveals clear traces of bed morphology, which indicates its strong effect on the wave field.

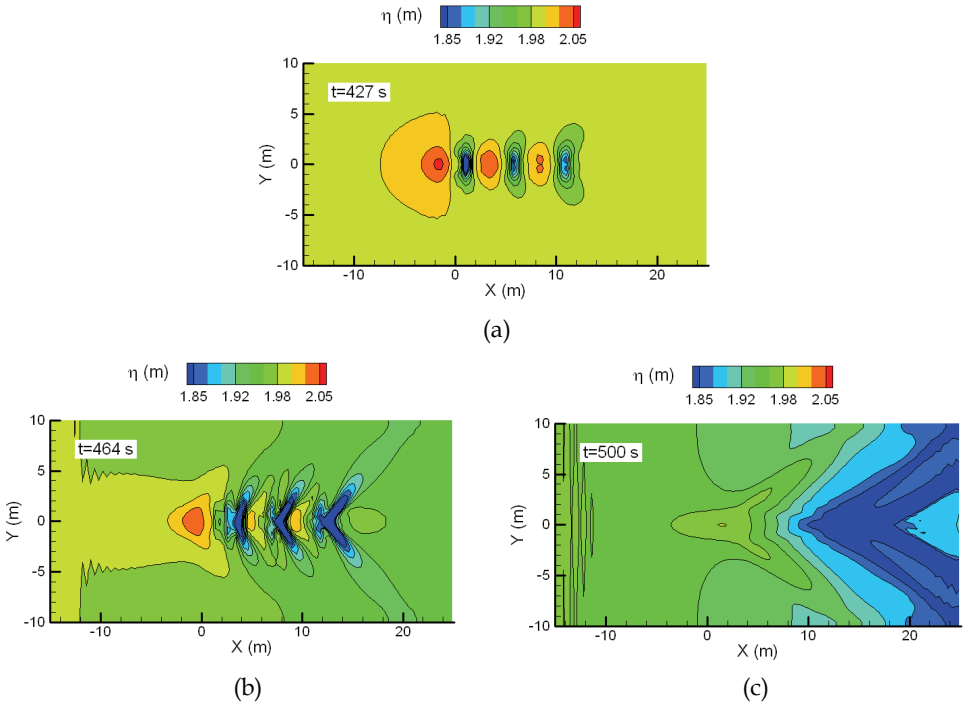

Fig. 13. Evolution of water surface elevation

Figure 15 shows the evolution of the heights and locations of three sand dunes as the wave is propagating towards the right. An interesting note is that the height of the first dune, the leading dune that is most upstream, decreases faster at the beginning (t < 470 s) in comparison with the heights of the other two dunes. As seen in Fig. 15a, however, at about t = 470 s the second and the third disappear or they merge with the first one, whereas the first still exists. After the disappearance of the second and third sand dunes, the height of the first dune remains about the same for a while. It is seen in Fig. 15b that, as all three dunes are about to merge with each other at t = 470 s, the first sand dune moves faster than the other two, with a large dx/dt, which accelerates the merging process.

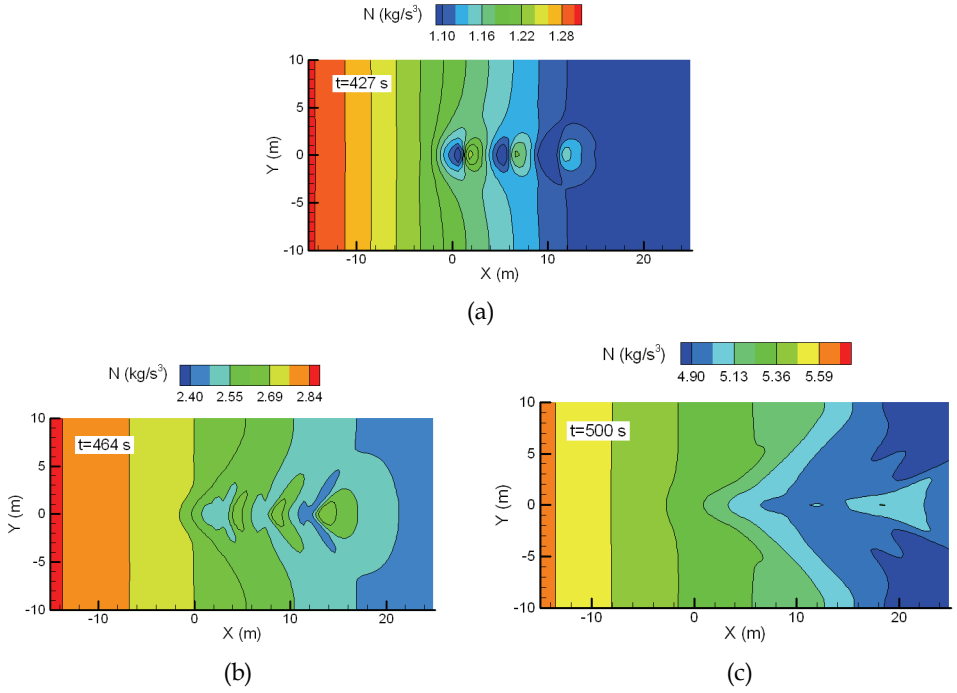

Fig. 14. Evolution of wave action

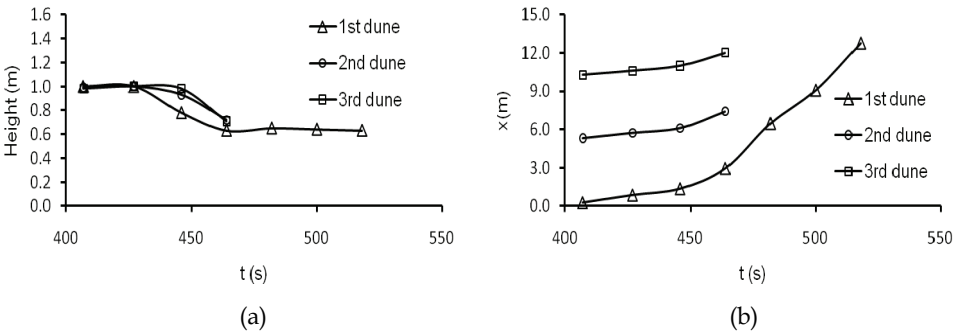

Fig. 15. Evolution of 3-dune. a) Heights of sand dunes. b) Location of sand dunes

Comparison of Figs. 12 through 14 with those obtained from modeling of single sand dunes (not shown) suggests that the evolution of a sand dune in the case of multiple sand dunes is consistent with a single sand dune in certain aspects, such as the shape of sand dunes (e.g., Hudson & Sweby, 2005; Tang et al., 2009). Nevertheless, sand dune development in situations of multiple sand dunes indeed behaves differently. In Fig. 16, the simulated results for situations of 1, 2, and 3 sand dunes (n = 1, 2, and 3 in Eq. 16) are presented, which shows the heights and locations of the leading or the most upstream sand dunes. The most interesting

finding in this figure is that, in case of multiple sand dunes, the heights of the leading sand dunes decrease slower but they move downstream faster. The larger the number of the sand dunes, the more pronounced this trend. It is also seen that the evolutions of heights and locations of the leading sand dunes in case of 2 and 3 sand dunes are not much different, but they are obviously distinct from that of an isolated sand dune (Fig. 16). This is a clear indication of the interaction between individual sand dunes and their resulting hydrodynamics.

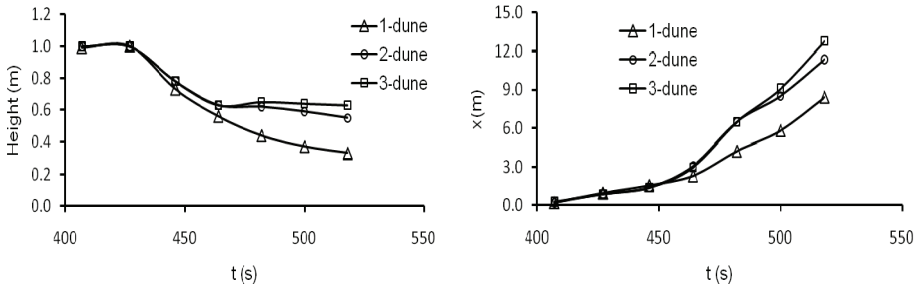

(a) (b)

Fig. 16. Evolutions of the leading sand dunes in case of 1-, 2-, and 3-dune. a) Heights of sand dunes. b) Locations of sand dunes

5. Concluding remarks

This chapter presents the needs to simulate multiscale and multiphysics coastal ocean hydrodynamics and the necessity to include its effects in estimation of seabed sediment scour and morphology evolution. It describes the multiscale and multiphysics method the authors proposed as a prominent approach, which is a hybrid method in conjunction with the domain decomposition method. The feasibility and potential of the approach in resolving multiscale and multiphysics processes is demonstrated using example computations.

The potential scour for the seabed diffuser indicates two important results: (1) the additional detail of the flow field computed by the CFD model is critical in capturing the areas of scour by tides; and (2) it is necessary to include waves for both mean and storm conditions to estimate the cumulative potential scour around the diffuser. The local scour problem can be computed using a high-resolution model but this would not permit an examination of variations within the seafloor area of interest. This is especially true for waves, which are sensitive to slight changes in water depth. The modeling of sand dunes illustrates the strong interaction between surface waves, currents, and morphology. The simulation presents interesting features of sand dunes with respect to their heights and locations, and it clearly indicates that evolution of multiple sand dunes is distinct from that of single sand dunes.

6. Acknowledgement

The first author was supported by PSC-CUNY Research Award. The second author was funded by the Office of Naval Research through the Naval Research Laboratory 6.1 Core program.

7. References

Alam, M. S., & Cheng, L. (2010). A parallel three-dimensional scour model to predict flow and scour below a submarine pipeline. *Central European Journal of Physics*, Vol. 8, pp. 604-619.

Ariathurai, R., Golden, J., Jr., McNally, W. H., Jr., Stout, G. A., & Neiheisel, J. (1983). Shoaling processes in navigable waters. *J. Waterway, Port, Coastal and Ocean Engineering*, Vol. 109, 199-221.

Benek, J. A., Steger, J. L., & Dougherly., F. C. (1983). A flexible grid embedding technique with application to the Euler equations. AIAA Paper 83-1944.

Blumberg, A. F., & Mellor, G. L. (1987). A description of a three-dimensional coastal ocean circulation model. In: Heaps, N. (Ed.), *Three-Dimensional Coastal Ocean Models*, American Geophysical Union, 1-16.

Booij, N., Ris, R. C., & Hoithuijsen, L. H. (1999). A third-generation wave model for coastal regions. I. Model description and validation. *J. Geophysical Research*, Vol. 104, C4, pp. 7649-7666.

Chen, C. S., Beardsley, R. C., & Geoffrey, C. (2006). An unstructured grid, finite-volume coastal ocean model FVCOM user manual. SMAST/UMASSD-06-0602.

Chen, C., Liu, H., & Beardsley, R. C. (2003). An unstructured, finite-volume, three-dimensional, primitive equation ocean model: application to coastal ocean and estuaries. *J. Atmospheric and Oceanic Technology*, Vol. 20, pp. 159-186.

Chiew, Y. M. (1991). Prediction of maximum scour depth at submarine pipelines. *J. Hydraulic Engineering,* Vol. 117, pp. 452-466.

Chui, C. K. (1992). *An Introduction to Wavelet*, Academic Press, Harcourt Brace Jovanovich, New York.

Dolbow, J., Khaleel, M. A., & Mitchell, J. (2004). *Multiscale Mathematics -- Initiative: A Roadmap*, PNNL-14966.

Fringer, O.B., Gerritsen, M., & Street, R.L. (2006). An unstructured-grid, finite-volume, nonhydrostatic, parallel coastal ocean simulator. *Ocean Modelling*, Vol. 14, pp. 139–173.

Ge, L., & Sotiropoulos, F. (2005). 3D unsteady RANS modeling of complex hydraulic engineering flows. Part I: Numerical model. *J. Hydraulic Engineering*, Vol. 131, pp. 800–808.

Halliwell, G. R. (2004). Evaluation of vertical coordinate and vertical mixing algorithms in the HYbird-Coordinate Ocean Model (HYCOM), Ocean Modeling, 7, 285-322.

Harten, A. (1993). Discrete multi-resolution analysis and generalized wavelets. *Applied Numerical Mathematics*, Vol. 12, pp. 153-192.

Heimusund, B. –O., & Berntsen, J. (2004). On a class of ocean model instability that may occur when applying small time steps, implicit methods, and low viscosities. *Ocean Modeling*, Vol. 7, pp. 135-144.

Henderson, F. M. (1966). Open channel flow, MacMillan Publishing Company, NY.

Hudson, J., & Sweby, P. K. (2005). A high-resolution scheme for the equations governing 2D bed-load sediment transport. *J. Numerical Methods Fluids*, Vol. 47, pp. 1085-1091.

Lax, P. D. (1954). Weak solutions of nonlinear hyperbolic equations and their numerical computation. *Communications On Pure And Applied Mathematics*, Vol. 7, pp. 159-193.

Lin, F. B., & Sotiropoulos, F. (1997). Assessment of artificial dissipation models for three-dimensional incompressible flows. *ASME J. Fluids Engineering Transaction*, 119, 331–40.

Keen, T. R., & Glenn, S. M. (1995). A coupled hydrodynamic bottom boundary-layer model of storm and tidal flow in the middle Atlantic Bight of North-America. *J. Physical Oceanography*, Vol. 25, pp. 391-406.

Keen, T. R., & Glenn, S. M. (1998). Resuspension and advection of sediment during Hurricane Andrew on the Louisiana continental shelf. *Proc. Fifth Int. Conf. Estuarine and Coastal Modeling*, Alexandria, Virgina, October 1997.

Keen, T. R., & Glenn, S. M. (2002). Predicting bed scour on the continental shelf during Hurricane Andrew. *J. Waterway Port Coastal and Ocean Engineering*, Vol. 128, pp. 249-257.

Keen, T. R., Stone, G., Kaihatu, J., & Hsu, Y. L. (2003). Barrier island erosion during a winter cold front in Mississippi Sound. *Proc. Coastal Sediments '03*, New Orleans, Louisiana, March 2002.

Kubatko, E. J. ,Westerink, J. J., & Dawson, C. (2006). An unstructured grid mophodynamics model with a discontinuous Galerkin method for bed evolution. *Ocean Modelling*, Vol. 15, pp. 71-89.

Kumar, P., & Foufoula-Georgiou, E. (1997). Wavelet analysis for geophysical applications, *Reviews of Geophysics*, Vol. 35, pp. 385–412.

Legeckis, R., Pichel, W., & Nesterczuk, G. (1983). Equatorial long waves in geostationary satellite observations and in a multichannel sea surface temperature analysis. *Bull. American Meteorological Society* , Vol. 64, pp. 133-39.

Luettich, R., & Westerink, J. (2004). Formulation and numerical implementation of the 2D/3D ADCIRC, Finite Element Model Version 44.XX. .

MacCormack, R.W. (1969). The effect of viscosity in hypervelocity impact cratering, AlAA Paper 69-354.

Mason, P. J. (1989). Large-eddy simulation of the convective atmospheric boundary layer. *J. Atmospheric Sciences*, Vol. 46, pp. 1491–1516.

Mei, C. C. (1983). *Applied Dynamics of Ocean Waves*. John Wiley & Sons.

Mellor, G. L., & Yamada, T. (1974). A hierarchy of turbulence closure models for planetary boundary layers. *J. Atmospheric Sciences*, Vol. 31, pp. 1791–1806.

Myrhaug, D., Ong, M. C., & Gjengedal, C. (2008). Scour below marine pipelines in shoaling conditions for random waves. *Coastal Engineering*, Vol. 55, pp. 1219-1223.

Papanicolaou, A. N., Elhakeem, M., Krallis, G., Prakash, S., & Edinger, J. (2008). The morphodynamic modeling of tidal sand waves on the shoreface. *J. Hydraulic Engineering*,Vol. 134, pp. 1–14.

Pedley, T. J. (1992). Hydrodynamic phenomena in suspensions of swimming microorganisms. *Annual Review of Fluid Mechanics*, Vol. 24, pp. 313-58.

Sleath, J. F. A. (1984). Sea bed mechanics, John Wiley & Sons, New York.

Smagorinsky, J. (1963). General circulation experiments with the primitive equations, I. The basic experiment, *Monthly Weather Review*, Vol. 91, 99-164.

Song, Y. T., & Hou, Y. T. (2006). Parametric vertical coordinate formulation for multiscale, Boussinesq, and non-Boussinesq ocean modeling. *Ocean Modeling*, Vol. 11, pp. 298-332.

Sotiropoulos, F., & Ventikos Y. (1998). Transition from bubble-type vortex breakdown to columnar vortex in a confined swirling flow. *Int. J. Heat Fluid Flow*, Vol. 19, pp. 446–58.

Sumer, B. M., Whitehouse, R. J. S., & Torum, A. (2001). Scour around coastal structures: A summary of recent research. *Coastal Engineering*, Vol. 44, pp. 153-190.

Tang, H. S., Jones, C., & Sotiropoulos, F. (2003). An overset grid method for 3D unsteady incompressible flows, *J. Computational Physics*, Vol. 191, pp. 567-600.

Tang, H. S., Keen, T. R., & Khanbilvardi, R. (2009). A model-coupling framework for nearshore waves, currents, sediment transport, and seabed morphology, Comm. *Nonlinear Sciences & Numerical Simulations*, Vol. 14, pp. 2935-2947.

Tang, H. S. Paik, J. Sotiropoulos, F., & Khangaokar, T. (2008). Three-dimensional CFD modeling of thermal discharge from multports. *J. Hydraulic Engineering*, Vol. 134, pp. 1210-1224.

Tang, H. S., & Wu, X. G. (2010). Multiscale coastal flow simulation using coupled CFD and GFD models, *Proc. Int. Congress Environ. Modeling & Simulation Software*, July 5-8, 2010, Ottawa, Canada.

Tolman, H. L. (1991). A third-generation model for wind waves on slowly varying, unsteady and inhomogeneous depths and currents. *J. Physical Oceanography*, Vol. 21, pp. 782–797.

Tonnon, P. K., van Rijn, L. C., & Walstra, D. J. R. (2007). The morphodynamic modeling of tidal sand waves on the shoreface. *Coastal Engineering*, Vol. 54, 279–296.

USGS (2010). http://pubs.usgs.gov/of/2000/of00-358/graphics/chapter2/midatlan.jpg.

Weller, R. A., Dean, J. P., Marra, J., Price, J. F., Francis, E. A., & Boardman, D. C. (1985). Three-dimensional flow in the upper ocean. *Sciences*, Vol. 227, pp. 1552-1556.

Wu, W. (2004). Depth-averaged two-dimensional numerical modeling of unsteady flow and nonuniform sediment transport in open channels, *J. Hydraulic Engineering*, Vol. 130, pp. 1013-1024.

Wu, X. G., & Tang, H. S. (2010). Coupling of CFD model and FVCOM to predict small-scale coastal flows, *J. Hydrodynamics*, vol.22, pp. 284-289.

Wunsch C., & Ferrari R. (2004). Vertical mixing, energy, and the general circulation of the oceans. *Annual Review of Fluid Mechanics,* Vol. 36, pp. 281–314.

Xu, J. S., Li, G. X., Dong, P., & Shi, J. H. (2010). Bedform evolution around a submarine pipeline and its effects on wave-induced forces under regular waves. *Ocean Engineering*, Vol. 37, pp. 304-313.

Xu, K. L, & Sun, G. (2009). Assessment of an interface conservative algorithm MFBI in a Chimera grid flow solver for multi-element airfoils. *Proceedings of the World Congress on Engineering. Vol II.* WCE 2009, July 1 - 3, London, U.K.

Younis, B. A., Teigen, P., & Przulj, V.P. (2001). Estimating the hydrodynamic forces on a mini TLP with computational fluid dynamics and design-code techniques. *Ocean Engineering*, Vol. 28, pp. 585–602.

Zamankhan, P., & Doolatshahi, A. A., (2008). Analysis of submarine pipeline scour using large-eddy simulation of dense particle-liquid flows. *Pipeline and Riser Technology; Ocean space utilization*, Vol. 3, pp 545-562.

Zang, Z., Cheng, L., Zhao, M., Liang, D., & Teng, B. (2009) A numerical model for onset of scour below offshore pipelines. *Coastal Engineering*, Vol. 56, pp. 458-466.